Influence of surface waviness in the heat generation and thermal expansion of the touchdown bearing

Neisi Neda, Heikkinen Janne, Sopanen Jussi

DOI: 10.1016/j.euromechsol.2018.10.014

Influence of surface waviness in the heat generation and thermal expansion of the touchdown bearing

Neda Neisi*), Janne E. Heikkinen, Jussi Sopanen

Department of Mechanical Engineering, Lappeenranta University of Technology, Skinnarilankatu 34, 53850 Lappeenranta, Finland.

Email: neda.neisi@lut.fi, janne.e.heikkinen@lut.fi, jussi.sopanen@lut.fi

Abstract

In an active magnetic bearings (AMBs) supported rotor system, the touchdown bearings have been proposed to support the rotor during an electromagnetic field shortage. The heat generation due to the high impact and collision of the rotor and touchdown bearing, in addition to the internal friction in the bearing, raises the temperature of the touchdown bearing. In this work, a numerical model is applied to simulate the rotor dropdown where the FE-model of the rotor is integrated with the dynamic and thermal model of the touchdown bearing. The rotor that is used as a case study is supported by a deep groove ball bearing and a pair of angular contact ball bearings installed in an X-configuration. The present study focuses on evaluating different orders of surface waviness in a pair of angular contact ball bearings. The equivalent electrical circuit model is implemented for computing the thermal behavior of the touchdown bearing. Results indicated that the dynamic friction coefficient between the rotor and inner race has a considerable impact on bounce height and the whirling motion of the rotor. Furthermore, for a certain amplitude of surface waviness, the effect of various orders of waviness is investigated and it has been found that surface waviness of the bearing alters the contact force and friction loss in the touchdown bearing. In addition, the effect of a higher amplitude of surface waviness on thermal expansion of the touchdown bearing is studied.

Keyword: touchdown bearing, rotor, dropdown, friction, thermal analysis, waviness

1 INTRODUCTION

The field of rotating electric machines has experienced a dramatic change from constant rotational speed machines to variable speed machines controlled by a frequency converter. Simultaneously, the rotational speeds have increased due to the advantages of higher rotational speeds. The highest rotational speeds can be achieved when the rotor can be rotated freely without mechanical contact with any other parts, even the bearings. This can be achieved using airfoil bearings that levitate the rotor on the air film, but this solution requires high rotational speeds to function and still the aerodynamic losses are noteworthy. The solution that is more promising is to levitate the rotor using a controlled electromagnetic field. In the active magnetic bearings (AMBs) supported system, electromagnetic forces levitate the rotor. The system does not suffer from wear due to this no-contact operation. Therefore, the AMBs are the preferred choice in high-speed applications compared to other bearing

types. Nevertheless, an AMB system requires a backup system for preventing fatal failures in case the electromagnetic field is lost due to electric short circuit or error in the control system.

Several studies have been conducted on rotor and touchdown bearing contact. As demonstrated by Kärkkäinen et al. [1] and Ecker [2], the high collision and friction forces in the dropdown will influence the whirling motion of the rotor. The nonlinear dynamic model of rotor casing rub has been extensively studied during the last century. A few well-known studies on rotor rub were performed by Taylor [3], Newkirk [4] and Childs [5]. Choy and Padovan [6] developed a theoretical model on the relation between rub force histories, energy levels, rub duration, incidence separation angles, as well as initiation of backward whirling. Muszynska [7], studied the rotor-stator rub theoretically and experimentally. Keogh [8,9] studied the contact of the rotor and the touchdown bearing, thermal bending of the rotor, and the effect of open loop and closed loop control systems for recovering the rotor levitation on AMBs. Recently, Liu et al. [10] developed a method based on signal processing to identify the orbit response of an AMB supported rotor during the bounce, and rub in the touchdown bearings. They applied the Fourier transform to identify the pendulum vibration and the full rub of the rotor. The previous study on the experimental and numerical rotor drop investigated by Schmied and Pradetto [11] indicated that because of the presence of electromagnetic force at the start of the dropdown test and also the time lag in the control system, the numerical result can deviate from the outcome of the experimental test.

Even though there has been considerable advancement in bearing technology, several cases of thermal failures of the bearings have been reported [12,13]. The reported failures were due to the rapid growth of the thermal induced preload and high-temperature gradient in the bearing. This type of failure can occur even without a considerable change in the vibration levels [13]. Numerous publications implemented the equivalent electrical circuit to study the heat transfer in the touchdown bearings [14-18]. Takabi and Khonsari [13,19] developed an experimental setup to evaluate the temperature in the conventional deep groove ball bearing. The experimental setup enabled them to investigate the variation of temperature under different speeds and operating conditions. The touchdown bearings utilized in an AMB supported rotor differ from the conventional rotor bearing system and the differences have been demonstrated in paper by Neisi et al. [20]. Due to the complicated geometry of the bearing assembly and the change in the heat generation rate, some simplifications for the boundary conditions and the model might be required. Accordingly, the result of the analytical solution might be slightly different from the experimental result [21]. In addition to the single-row bearings, the thermal analysis of double-row bearings has been studied. Yan et al. [22] and Ai et al. [23] performed the thermal analysis of the double-row tapered roller bearing. Jin et al. [17] compared the thermal structure of the single-decker and double-decker touchdown bearings. They presented a model for improving the rotational speed of the intermediate race of the double-decker ball bearing. They concluded that the double-decker configuration decreases the temperature rise in the touchdown bearing. The aforementioned publications on the thermal model of the touchdown bearing presume that the bearing is installed in an ideal condition. However, as a result of the surface waviness, particularly due to the wear between rotor and touchdown bearing in the previous dropdown of the rotor, the friction torque and the power loss calculated for the thermal model of the touchdown bearing can be different from the ideal condition of the bearing. As stated in the standard API 617, the touchdown bearing should withstand a minimum of two full dropdowns

from maximum continuous speed to zero speed and a minimum of ten partial contacts due to disturbances in the system exceeding the force capacity of the AMBs [24].

The waviness in the bearing can be considered as one of the main reasons for bearing vibration. There are numerous studies about bearing waviness in a conventional ball bearing. Zhuo et al. [25] evaluated the influence of applied load, internal clearance, number of balls as well as surface waviness on the kinematic behavior of a double-row self-aligning ball bearings. They described the vibration characteristic of the rotor bearing system including surface waviness in the bearing races. The influence of the surface waviness on the stability of a rigid rotor supported by ball bearings is presented in a paper by Harsha and Kankar [26]. They showed that the nonlinear vibration response of the rotor bearing system due to the surface waviness in the bearing system is highly affected by the number of balls and order of waviness. In addition, they pointed out that by increasing the number of balls, the stiffness of the system will be higher and the influence of ball pass frequency decreases. Wardle [27,28] conducted both a mathematical and experimental study on the frequency response and vibration analysis of the bearing having surface waviness. The study by Changqing and Qingyu [29] on the effect of internal clearance and waviness includes the high-speed effect, and their work indicated that the waviness causes the change in the frequency of the peak of amplitude. Liu et al. [30] developed a multibody dynamic model for a ball bearing. They found that as a consequence of the high-speed effect in the bearing, the waviness in the outer race has a higher influence on the vibration of the system rather than the waviness in the inner race. The aforementioned publications on the surface waviness in the bearing mainly discuss the influence of surface waviness, theoretically. A recent paper by Heikkinen et al. [31] evaluates the vibration analysis of a spherical roller bearing from surface waviness both experimentally and numerically.

Few studies have focused on the influence of the waviness in touchdown bearing application. Recently, Halminen et al. [32,33] developed a multibody model of the touchdown bearing including surface waviness. They investigated the effect of 1st, 2nd and 3rd order surface waviness in the bearing races in the calculation of the friction loss in the touchdown bearing. It is possible to acquire further improvement in the touchdown bearing design by considering the influence of the surface waviness in the dynamic and thermal model of the touchdown bearing. With this goal, the present study aims to apply the simple model for the ball bearing to evaluate the contact force and power loss in a rotor drop. Moreover, the influence of friction heat generated in the touchdown bearing due to different orders of surface waviness in bearing rings will be identified. Furthermore, this work presents the impact of the waviness on the temperature rise in the bearing during rotor drop.

2 MODEL OF THE ROTOR

The FE-model of the rotor of a high-speed electric motor depicted in Fig. 1 has been constructed based on the shear deformable Timoshenko beam element that was used for rotating shafts by Nelson [34]. In regular operation of the machine, the rotor is levitated in the electromagnetic field and AMBs carry the weight of the rotor and the operational loads. The equation of motion of the system can be written as:

$$\mathbf{M}\ddot{\mathbf{X}}+(\mathbf{C}+\omega\mathbf{G})\dot{\mathbf{X}}+\mathbf{K}\mathbf{X}=\omega^2\mathbf{Q}_1+\mathbf{Q}_2 \quad (1)$$

In the equation of motion, **M** defines the mass matrix, **C** is damping matrix and **K** represents the stiffness matrix. The gyroscopic matrix is denoted by **G**. The vector of the generalized coordinate is shown by **X**. The vector $\mathbf{Q_1}$ is vector of nodal unbalance and the vector of externally applied force is denoted as $\mathbf{Q_2}$ and ω is the angular rotation speed of the rotor.

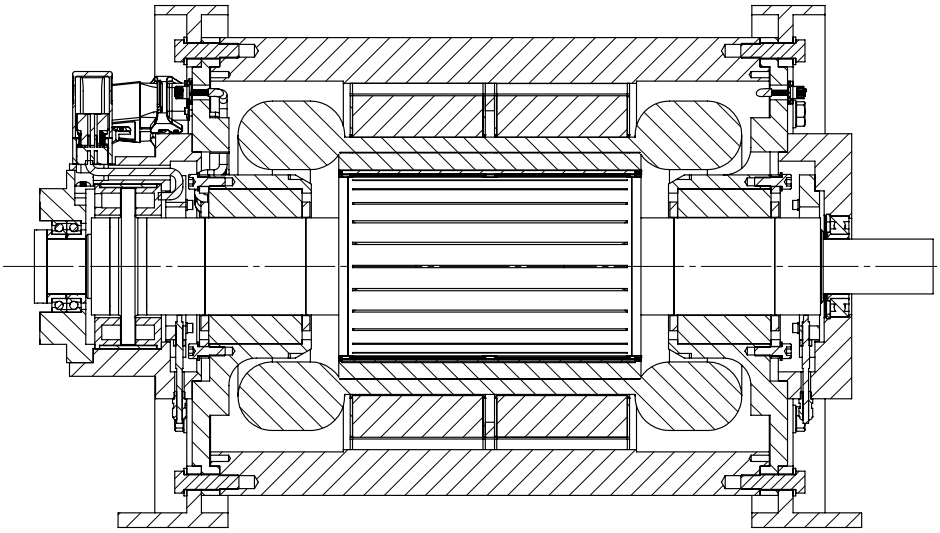

Fig. 1. A case study of the electric motor.

3 MODEL OF A TOUCHDOWN BEARING

The touchdown bearings are simulated utilizing the model for the ball bearing developed by Sopanen and Mikkola [35]. The relative displacement between bearing rings is as follows:

$$e_j^r = e_x \cos\beta_j + e_y \sin\beta_j \tag{2}$$
$$e_j^t = e_z - \left(\psi_x \sin\beta_j + \psi_y \cos\beta_j\right)(R_{in}+\varepsilon_{in}+r_{in})$$

where e_x, e_y and e_z feature the relative displacements between the bearing races along main axes. The index j represents the ball number. β_j is the azimuth angle of j^{th} ball. In Fig. 2, the inner race radius and inner race groove radius are denoted as R_{in} and r_{in}, respectively. The tilting of the inner race in principle directions are denoted as ψ_x and ψ_y. The distance between the bearing rings is given by:

$$D_j = r_{out}+r_{in} - \frac{(R_{in}+\varepsilon_{in})+r_{in}+e_j^r - (R_{out}+\varepsilon_{out})+r_{out}}{\cos\varphi_j} \tag{3}$$

where the contact angle is denoted as φ_j:

$$\varphi_j = \tan^{-1}\left(\frac{e_j^t}{R_{in}+\varepsilon_{in}+r_{in}+e_j^r - R_{out} - \varepsilon_{out}+r_{out}}\right) \tag{4}$$

where ε_{in} and ε_{out} represent the thermal expansion of the inner race and outer race, respectively. In the dropdown, based on the relative displacement of the rotor and inner ring, the contact angle, φ_j , can be slightly different from the nominal contact angle of the bearing mentioned in the bearing catalogue.

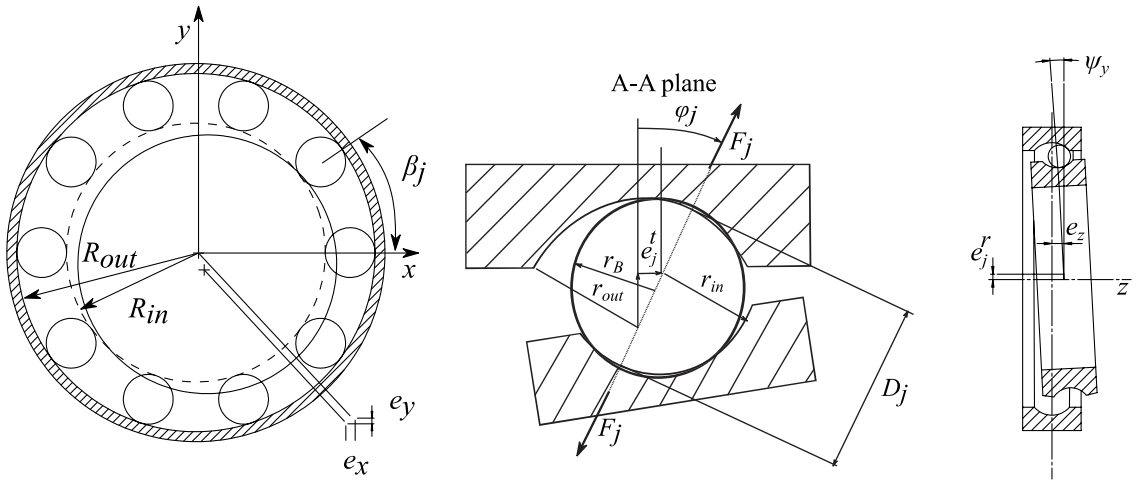

(a) (b) (c)

Fig. 2. Cross-section of the ball bearing.

The total elastic deformation of the inner race is as follows:

$$\delta_j^{tot}=d_j+\varepsilon_b-D_j \tag{5}$$

where ε_b is thermal expansion of balls. Then, the contact force between ball j^{th} and inner race can be obtained by Hertzian contact theory [1]:

$$F_j=K_b\left(\delta_j^{tot}\right)^{3/2} \tag{6}$$

The detailed calculation of total contact stiffness, K_b , is presented in previous publications [35].

3.1 Model of the contact

The radial contact force between rotor and touchdown bearing is calculated based on the nonlinear contact model introduced by Hunt and Crossley [36] and the energy dissipation during the impact is taken into account:

$$F_r=\begin{cases} K\delta^n+b\delta^n\dot{\delta}^q & ;e_r>c_r \text{ and } F_r>0 \\ 0 & ;e_r\le c_r \text{ and } F_r\le 0 \end{cases} \tag{7}$$

where K represents the contact stiffness between the rotor and inner race, q=1 and n is a constant dependent on the type of the contact (for the contact between the rotor and touchdown bearing n=10/9) and $\dot{\delta}$ is the rate of indention. The damping parameter (b) can be related to the coefficient of restitution which is defined as the ratio of relative velocity before and after collision of the bodies. Hunt and Crossley [36] showed that $b=\frac{3}{2}\lambda K$ and they

pointed out that the contact parameter λ ranged between 0.08 and 0.32 sec/m can be reasonable. If λ is very low, the material will be very resilient. On the other hand, very large value of λ as 0.64 sec/m can raise questions in the assumption for deriving $b = \frac{3}{2}\lambda K$ and might not be appropriate. This method has been also used in simulation of the dropdown by Sun [18]. For the steel the coefficient λ ranges 0.08 and 0.2 [18]. In present study the contact parameter λ equal to 0.08 has been used in the simulation.

The penetration of the rotor in the inner race can be obtained as:

$$\delta = e_r - c_r + \varepsilon_{in} \tag{8}$$

where the radius of the air gap between the rotor and touchdown bearing is denoted as c_r. In the modified Hertzian contact model, the velocity of penetration of the rotor in the touchdown bearing, $\dot{\delta}$, has been taken into account. The following equation can be used to obtain the radial displacement of the rotor [1]:

$$e_r = \sqrt{e_{x,r}^2 + e_{y,r}^2} \tag{9}$$

where the radial displacement between the rotor and the inner race along the x- and y-axis are denoted as $e_{x,r}$ and $e_{y,r}$. The friction force between the rotor and inner race is given by:

$$F_\mu = \mu F_r \tag{10}$$

where μ is the friction coefficient between the rotor and inner race. The comparative study on the effect of the friction coefficient and the friction model in the simulation of the rotor dropdown presented in the study of Kärkkäinen et al. [1] indicated that the Coulomb Mohr friction model with the constant friction is able to provide acceptable results for the dynamic simulation of rotor dropdown. The assumption of constant friction coefficient has been made for the simulation since, the dropdown occurs in a short time interval and it was expected that not significant change in friction coefficient happens. Furthermore, the sensitivity analysis for the influence of different values of the dynamic friction coefficient on the temperature rise of inner ring of touchdown bearing shows that there is a small change in the temperature rise of inner ring due to increasing the friction coefficient [17]. It is important to note that the friction coefficient is not the only parameter affecting the heat generation in the touchdown bearing and the temperature rise is influenced by additional parameters as: geometry and structure of rotor, bearing and support properties as well as the angular velocity of rotor in the start of dropdown. Beside that during the life time of the touchdown bearing due to the wear between rotor and inner ring the friction can increase.

Considering the contact model and the bearing model introduced earlier, the mechanical model for the interaction of the rotor and touchdown bearing is introduced in Fig. 3. F_r and F_μ are the normal and tangential force in the contact of the rotor and touchdown bearing. The forces can be obtained from equations 7 and 10 respectively. K_{sup}

and C_{sup} represent the support stiffness and damping. The damping of the bearing C_b typically ranges (0.25-2.5)·10-5 bearing stiffness K_b [37]. Defining the support stiffness and damping parameters is not straightforward, but they can be obtained experimentally or using FE analysis. M_v is friction drag torque (load dependent friction torque) that will be demonstrated in section 3.4. ω_i and ω_r represent the angular velocity of inner race and rotor, respectively.

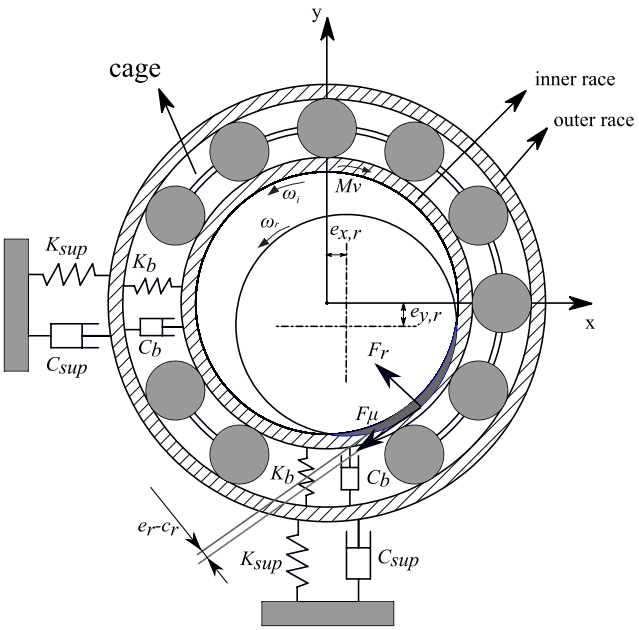

Fig. 3. Mechanical model for interaction of the rotor and touchdown bearing.

3.2 Modeling of surface waviness

The waviness imperfection refers to the dimensional irregularity where the bearing surface periodically deviates from the nominal dimension. Hence, it can influence the total elastic deformation of the bearing race. Consequently, it can change the contact force in the touchdown bearing. The surface waviness in the bearing can be modeled using the sinusoidal function as follows:

$$A_{in}=A\sin(m\beta) \tag{11}$$

where A is amplitude, m is order of waviness and β is azimuth angle of the bearing (Fig. 4).

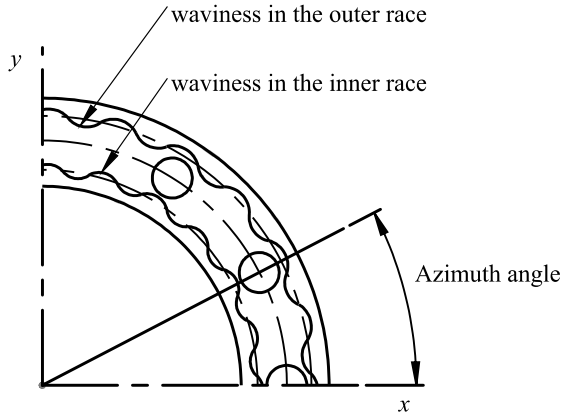

Fig. 4. Model of surface waviness in bearing races.

Therefore, the elastic deformation of the bearing race can be rewritten as:

$$\delta_j^{tot}=d_j+\varepsilon_b-D_j+\sum_{N_w=1}^{n}A_m^{in}\sin(m^{in}(\beta)+\theta_{irw})+\sum_{N_w=1}^{n}A_m^{out}\sin(m^{out}(\beta)+\theta_{orw}) \tag{12}$$

where m is waviness order and θ_{irw} and θ_{orw} are the phase angels of m^{th} order waviness of the inner race and outer race, respectively. In practice, it is possible that the surface waviness in the bearing will be a combination of different waves. Therefore, the amplitudes of the various number of waves (n) are summed.

3.3 Bearing Kinematic

In the high-speed bearing, the spinning of the ball around its axis can be considered as one of the sources of the friction generated in the bearing. Applying the instant center of velocity and trigonometry relation, the spinning velocity of the ball can be derived [38]. The angular speed of the ball in the contact area between ball/inner race (ω_{ci}) and ball/outer race (ω_{co}) intersect each other at the point P along the axis of the bearing (Fig. 5).

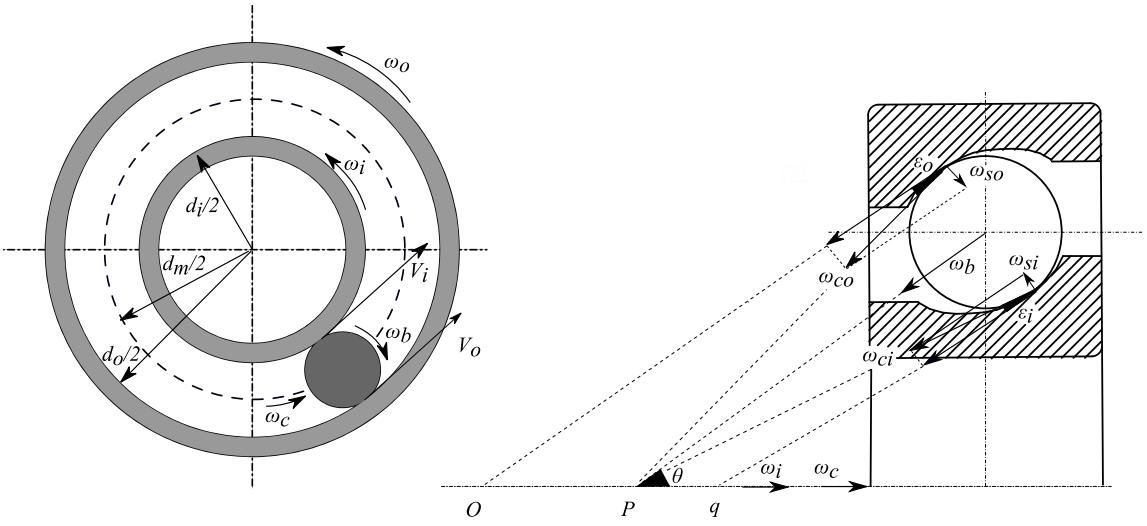

Fig. 5. Spinning velocity in the ball bearing.

The spinning velocity in the contact of ball and bearing races is as follows [39]:

$$\begin{aligned}\omega_{si}&=-\omega_b\sin(\varphi_i-\theta)+\omega_{ci}\sin(\varphi_i)\\ \omega_{so}&=\omega_b\sin(\varphi_o-\theta)+\omega_{co}\sin(\varphi_o)\end{aligned} \tag{13}$$

where φ_i and φ_o represents the contact angle in inner race and outer race, respectively. The ball pitch angle is denoted as θ:

$$\tan\theta = \frac{\sin\varphi_o}{\cos\varphi_o + d_b/d_m} \tag{14}$$

and ω_b is the angular speed of ball and it can be calculated as follows [40]:

$$\omega_b = \frac{\omega_{co}(d_m + d_b\cos\varphi)}{d_b} \tag{15}$$

where d_b and d_m represent the ball diameter and pitch diameter, correspondingly.

3.4 Thermal model of bearing

In the touchdown bearing, heat transfers by both conduction and convection heat transfer mechanisms. The friction between the rotor and the inner race, and also the friction heat generated between the ball and bearing races, are considered as heat sources. Previous studies [15-18] presented the one-dimensional heat transfer model for the thermal model of the touchdown bearings. Fig. 6 shows a schematic of the equivalent electrical circuit of the thermal model.

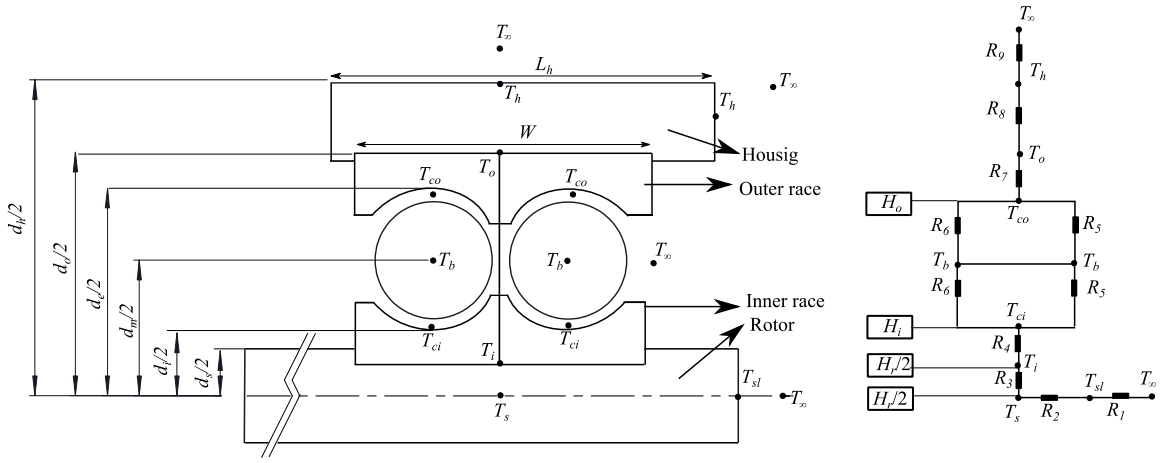

Fig. 6. Equivalent electrical circuit model of the bearing.

The thermal resistances are summarized in Table 1. Where d_b , d_h, d_i, d_o, d_s, d_o, L_h and W are the dimensions of the bearing that can be found from the bearing catalog and the drawings of the case study. H_i, H_o and H_r represent the heat generation in the inner ring, outer ring and in the contact of rotor and touchdown bearing, respectively and that will be described in section 3.5.

Table 1: Thermal resistance of bearing elements [16].

Shaft/Inner race	Ball/ambient	Outer race	Housing
R_1 convection	R_5 conduction	R_7 conduction	R_8 conduction
R_2 conduction	R_6 convection		R_9 convection
R_3 conduction			
R_4 conduction			

The following equation represents the coefficient of free convection heat transfer from the bearing housing [41]:

$$h_h=23(T-T_\infty)^{0.25} \tag{16}$$

where T is temperature and T_∞ is the ambient temperature.
The heat transfer balance should be satisfied in each node of the model [16].

$$H_{in}-H_{out}=\rho CV\frac{dT}{dt} \tag{17}$$

where H_{in} and H_{out} are input and outflow power loss, respectively. C is the specific heat , ρ is the density and V is the volume. The temperature gradient is denoted as dT/dt. In a discrete form, the thermal balance in the bearing can be rewritten as [17].

$$\mathbf{M}_{\text{brg}}\mathbf{C}_{\text{brg}}\left(\mathbf{T}^{\text{t}+\Delta\text{t}}-\mathbf{T}^{\text{t}}\right)=\left(\mathbf{H}_{\text{in}}^{\text{t}}-\mathbf{H}_{\text{out}}^{\text{t}}\right)\Delta\text{t} \tag{18}$$

where $\mathbf{M}_{\text{brg}}$ is lumped mass matrix and $\mathbf{C}_{\text{brg}}$ is a matrix form of the specific heat for the bearing model. The input heat flux and output heat flux are denoted as $\mathbf{H}_{\text{in}}^{\text{t}}$ and $\mathbf{H}_{\text{out}}^{\text{t}}$, correspondingly. The temperature in new time step ($\mathbf{T}^{\mathbf{t}+\Delta\mathbf{t}}$) can be obtained by the temperature in the previous time step ($\mathbf{T}^{\text{t}}$).

3.5 Calculation of Power Loss in Dropdown

As mentioned earlier, the friction between the rotor and the inner race besides the friction inside bearing are considered as heat sources. The power loss resulting from the contact between the rotor and inner race can be expressed as follows [17]:

$$H_r=F_{frc}V_{rel} \tag{19}$$

where V_{rel} is the relative velocity between rotor and inner race and F_{frc} is the friction force between the rotor and touchdown bearing. The second part of the power loss is due to friction between the balls and the races. The equation that expresses the global friction in the bearing (M) is as follows [41]:

$$M=M_L+M_v \tag{20}$$

The load-dependent term is given by [42]:

$$M_L=f_1Pd_m \tag{21}$$

where P is the equivalent load of the ball bearing. The velocity-dependent term can be calculated by [42]:

$$\begin{cases} M_v = 10^{-7} f_2 (vN)^{2/3} d_m^3 & vN > 2000 \\ M_v = 160 \times 10^{-7} f_2 d_m^3 & vN \leq 2000 \end{cases} \tag{22}$$

where, f_1 and f_2 are factors dependent on the design of the bearing and the load on the bearing, v is kinematic viscosity (centistoke) and N is speed of inner race (rpm) and d_m presents the pitch diameter (mm). In high-speed application, the spinning torque, as a consequence of the spinning movement of the individual balls around its own axis, cannot be neglected. The spinning torque in the inner ring can be expressed as follows [43]:

$$M_{si} = \frac{3\mu F_j a \bar{\zeta}}{8} \tag{23}$$

where μ is the friction coefficient, F_j is contact force given in equation (6). The parameter $\bar{\zeta}$ is the elliptical integral of second type. The equation that describes the total heat generation at the inner race is as follows [16]:

$$H_i = \sum_j H_{ij} = \sum_j \left(\omega_b M_{ij} + \omega_{si} M_{si} \right) \tag{24}$$

where, M_{ij} is the friction torque in the inner race and M_{si} is spinning drag torque. A similar approach can be applied to obtain the total heat generation at the outer race.

3.6 Bearing Deformation Under Thermal Effect

As a result of variation in the temperature, the dimension of the bearing components can be changed. The thermal expansion of ball and inner race are expressed as [18]:

$$\varepsilon_b = \alpha_b r_b T_b \tag{25}$$

$$\varepsilon_{in} = \frac{\alpha_i}{3} \frac{(1+v_i) r_s}{r_i + r_s} [\Delta T_i (2r_s + r_i) + \Delta T_{ci} (2r_i + r_s)] \tag{26}$$

The radius of the ball, inner race and cross section of rotor in the location of the touchdown bearing are denoted as r_b, r_i and r_s, respectively. The thermal expansion coefficient of the ball and inner race are expressed as α_b and α_i, respectively. v_i is the Poisson's ratio of the inner ring. The temperature of the ball is denoted as T_b, and ΔT_i is the difference between the temperature of the inner ring and ambient temperature. Likewise, ΔT_{ci} shows the corresponding value for the contact area of the ball/inner ring.

Calculation of the radial thermal expansion of the outer race is as follows [18]:

$$\varepsilon_{out} = \frac{\alpha_o}{3} \frac{(1+v_{out}) r_{out}}{r_{out} + r_h} [\Delta T_{out} (2r_{out} + r_h) + \Delta T_h (2r_h + r_{out})] \tag{27}$$

In the above equation, r_{out} and r_h refer to the radius of the outer race and housing, respectively. α_o is the thermal expansion coefficient of the outer race and v_{out} is the Poisson's ratio of the outer race. The difference between the

temperature of the outer race and housing with the ambient temperature are denoted as ΔT_{out} and ΔT_h, correspondingly.

The following equation gives the total radial interface in the bearing [16]:

$$\varepsilon_t = \varepsilon_b + \frac{(\varepsilon_{in} - \varepsilon_{out})}{2} \cos\varphi \tag{28}$$

The data from the thermal expansion of the bearing are required to obtain the thermal preload of the bearing which will be described in the following section.

3.7 Updating the Model

The material of the bearing and the geometry will be designated in a way that there should be a balance between the heat generation inside the bearing and the heat dissipated from the bearing. If the heat dissipation is less than the heat generated inside the bearing, the temperature in the bearing will rise and it can promote the possibility of thermal failure. Therefore, it is essential to update the thermal effect in the model and include the effect of thermal expansion in equations (2)-(5) and (8). The flow chart of the simulation is presented in Fig. 7.

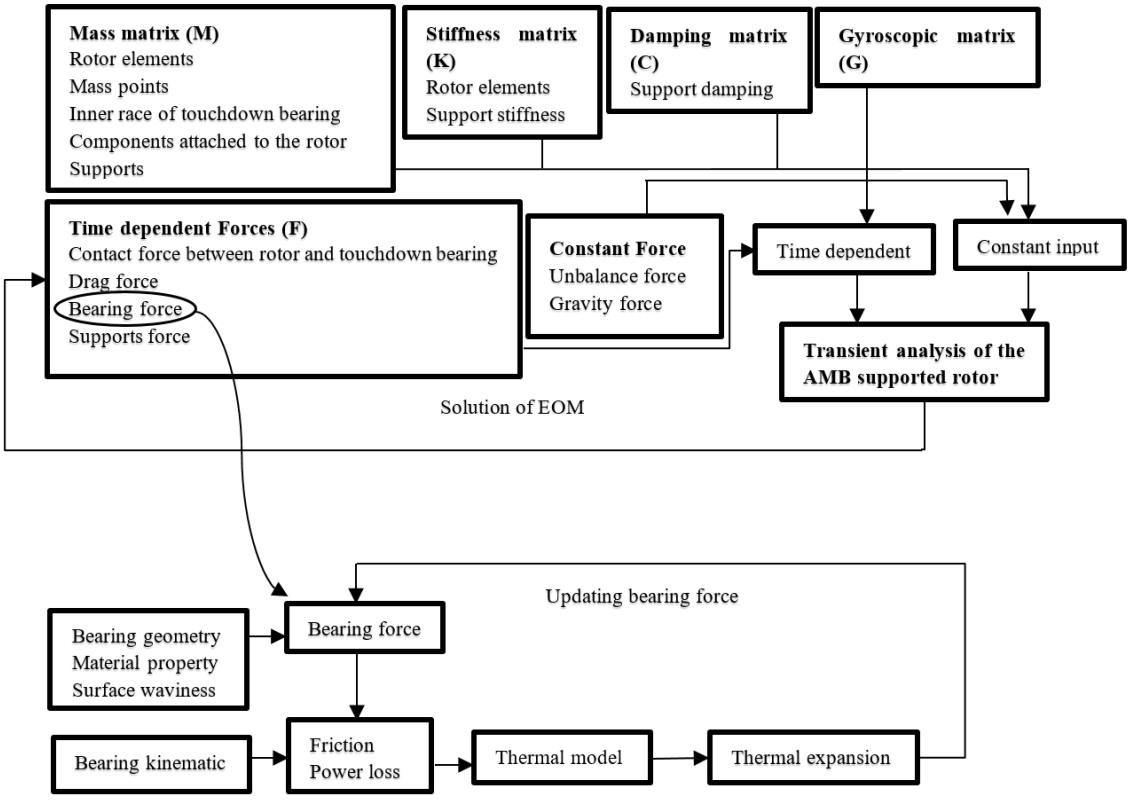

Fig. 7. Flowchart of updating bearing load in the AMB supported rotor.

4 CASE STUDIES AND RESULTS

The parameters required to analyze the case study of a rotor are shown in Table 2. The main dimensions of the rotor are depicted in Fig. 8-a. The touchdown bearings 1 is a hybrid deep groove ball bearing of the type 6014

HC5/C3 and touchdown bearing 2 is a pair of angular contact ball bearings of the type 71914-E-T-PS4 installed in an X-configuration, the technical data of bearing are shown in Table 3. Fig. 8-b shows the FEM model of the rotor main shaft and the location of the touchdown bearings. The rotor FE model includes 31 rotor nodes. The bearing coordinate system shown in Fig. 2 differs from rotor coordinate system that is considered by using a transfer matrix for bearing forces. In the FE model, the touchdown bearings are located at nodes 2 and 28. The connection gear (node 1), axial AMB (node 5), axial AMB nut (node 3), nuts for radial AMB rotor stacks (nodes 7, 25), radial AMB rotor stacks (nodes 10, 22) are modeled as mass points. A conservative modeling approach was used and only the main shaft is modeled as beam elements whereas all the surface elements are included as mass elements neglecting the stiffness of the components contributing to the total rotor stiffness. The copper end-rings in the rotor are also considered as mass points at nodes 13 and 19. The detail figure for the mechanical interaction of the rotor and touchdown bearing is shown in Fig. 3.

The FEM model of the rotor is validated using experimental modal analysis by obtaining the bending frequencies of the rotor. The lowest bending mode frequency of the rotor without actuators such as impellers was 673.5 Hz [44]. The FE model of the rotor is created in self-made MATLAB rotordynamics toolbox. The transient analysis was performed using a ready-made ode45 integrator that is based on 4th order Runge-Kutta integration method. The simulation time was 0.3 seconds using a time step of 1e-5 s, the maximum integration step was 5e-6 s and the maximum allowable integration error 1e-5."

The support stiffness was obtained by FEM analysis and the damping was estimated using FE modal analysis and damping ratio of 1 % that is typical for steel structures. The effective mass for the support stiffness was obtained using FE modal analysis and 3D model of the structure by obtaining the moving part of the structure at first mode and defining the corresponding inertia properties from 3D model. The unbalance masses are obtained from balancing results of a low speed balancing of the prototype machine and balancing planes are used for unbalance locations. The value used for the static and dynamic contact friction is selected from the literature [17].

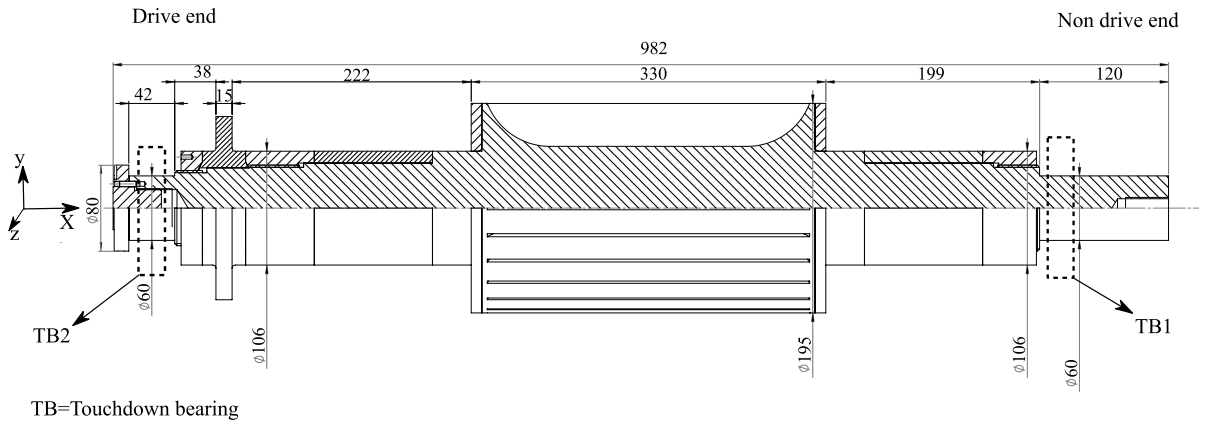

a)

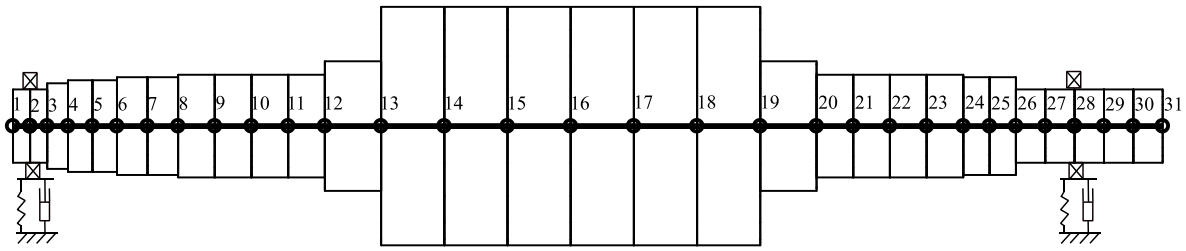

b)

Fig. 8. The main dimensions and FEM model of the electric motor rotor/touchdown bearing. a) Dimension, b) FEM model of rotor

Table 2. The main data for the simulation of the rotor dropdown.

Initial rotation speed of the rotor	15200 rpm
Modulus of elasticity of steel part of rotor	$2.0 \cdot 10^{11}$ Pa
Material density of steel part of rotor	7850 kg/m^3
Poisson's ratio of steel part of rotor	0.3
Modulus of elasticity of radial AMB lamination of rotor	$1.85 \cdot 10^{11}$ Pa
Material density of radial AMB lamination of rotor	7600 kg/m^3
Poisson's ratio of radial AMB lamination of rotor,	0.285
Mass of rotor	109.7 kg
Effective mass of support, NDE	50 kg
Support stiffness of NDE (K_y, K_z)	$(1.5, 1.1) \cdot 10^9$ N/m
Effective mass of support, DE	85 kg
Support stiffness of DE (K_y, K_z)	$(2.7, 1.5) \cdot 10^9$ N/m
Support damping of NDE (C_y, C_z)	$(2.82) \cdot 10^3$ Ns/m
Support damping of DE (C_y, C_z)	$(3.68) \cdot 10^3$ Ns/m
Contact stiffness between rotor and inner race (bearing 1)-TB1	$1.144 \cdot 10^9$ N/m$^{1.11}$
Contact stiffness between rotor and inner race (bearing 2)-TB2	$1.73 \cdot 10^9$ N/m$^{1.11}$
Radial Air gap between rotor and touchdown bearings	250 µm
Polar moment of inertia of rotor	0.39 kgm^2
Diameter moment of inertia of rotor	4.5535 kgm^2
Unbalance mass at AMB disk	$1.07 \cdot 10^{-6}$ kg·m @ 180°
Unbalance mass at the center of the rotor active part	$2.78 \cdot 10^{-6}$ kg·m @ 180°
Static contact friction coefficient between rotor and inner race	0.05
Dynamic contact friction coefficient between rotor and inner race	0.1

Table 3. Bearing data, bearing type 71914-E-T-PS4

Bore diameter	70 mm
Outside diameter of inner race	78 mm
Inside diameter of outer race	100 mm

Outside diameter of outer race	110 mm
Pitch diameter	85 mm
Bearing width (for one row)	16 mm
Housing axial width (for one row)	25 mm
Housing diameter	120 mm
Nominal contact angle	25 degree
Number of balls	23

Thermal properties	Ceramic	Steel
Thermal conductivity of race (W/mK)	35	70
Linear expansion coefficient	3.2·10-6	11.8·10-6
Linear expansion coefficient		
Poisson's ratio	0.3	0.26
Density	3200	7800
Modulus of elasticity	3.15·1011 Pa	2.0·1011 Pa
specific heat capacity (J/kgK)	673	510
kinematic viscosity of air (m^2/s)	$1.5 \cdot 10^{-5}$	

4.1 Orbital motion of rotor

The orbital motions of the rotor for three different dynamic friction coefficients between the rotor and touchdown bearings are shown in Fig. 9. It can be seen in Fig. 9 (a-c) that after the initial impact of the rotor with touchdown bearings, the rotor bounces back up to the height more than half of the air gap. The simulation result revealed that the friction has a visible influence on the orbital motion. As can be seen in Fig 9-a, with the low value of the friction coefficient as 0.05, after the second contact of the rotor and touchdown bearing number 2 (TB2), the rotor bounces up to approximately -150 µm. As the friction between the rotor and touchdown bearing increases to 0.1 and 0.15, the rotor impacts the touchdown bearing at a point where the arc length is wider and the rotor gradually settles toward the right and the magnitude of the bounce height decreases (Fig 9-b,c).

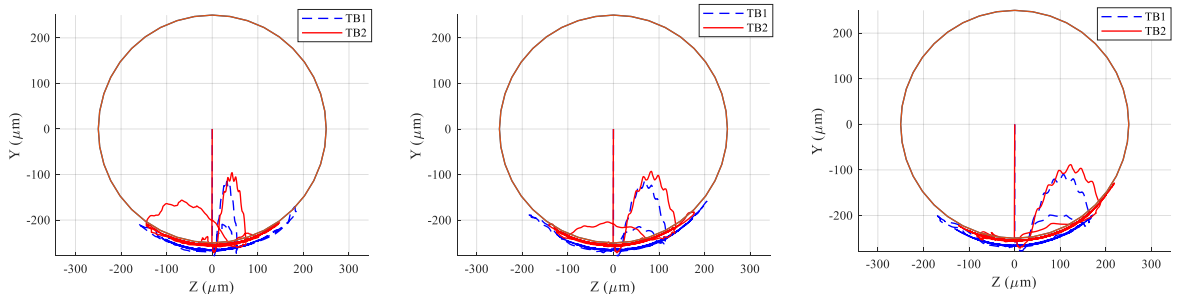

a) b) c)

Fig. 9. The orbital motion of a rotor for different values of dynamic friction coefficient between rotor and inner race: a) 0.05 b) 0.1 c) 0.15.

In the FE-model of the rotor, the *x*-axis is defined along the longitudinal axis of the rotor (Fig. 8). This work focuses on studying the deformations and contact forces in the bearing plane (*y*- and *z*-directions) and the axial deformations are not considered. Fig. 10 shows the displacements in *y*- and *z*-directions of the rotor at the locations of touchdown bearings during a touchdown event using the friction coefficient listed in Table 2. The first hit of the rotor on the touchdown bearings deforms both bearings and support, resulting in higher displacement than 250 µm that is the air gap length of the touchdown bearings. After the first hit, the rotor lifts off from the inner ring and during the subsequent contacts the displacement in the vertical direction is reduced (Fig. 10 (a)) and gradually the rotor will stabilize on the bottom of the bearing inner ring having a total displacement slightly higher than the air gap length. The contacts of the rotor with the touchdown bearings can be also seen from the *z*-displacement (Fig. 10 (b)). In this direction, the displacement is not exceeding or even approaching very close to the air gap length. The results curve indicates a smooth swinging motion on the bottom of the bearing inner ring, decreasing gradually in the direction of the gravity (0 displacement in the *z*-direction).

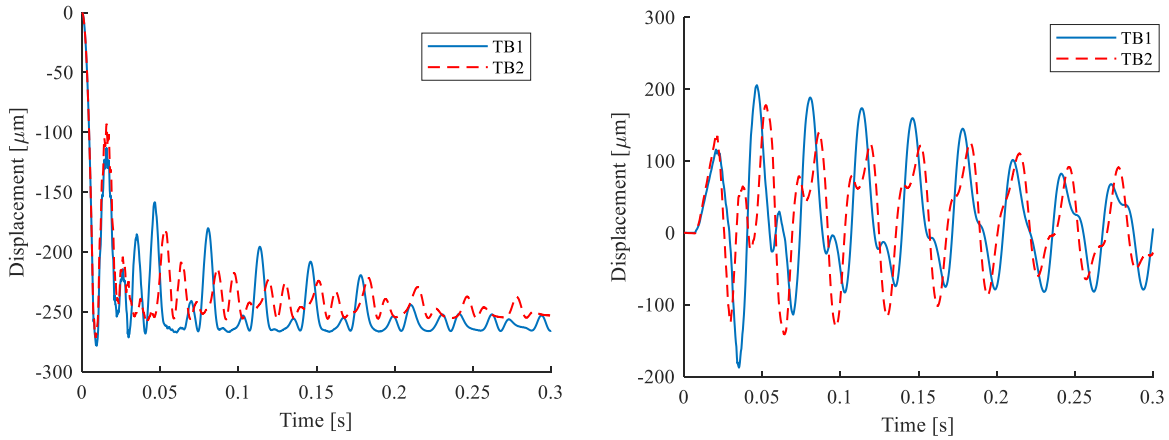

Fig. 10. The displacement of rotor at touchdown bearing location: a) *y*-direction b) *z*-direction.

Fig. 11 shows angular velocities of the inner rings in both bearings. As can be seen, the inner rings of the touchdown bearings accelerate with different rates. That is mainly due to the different bearing types having different inertia properties. The touchdown bearing 1 is a deep groove ball bearing that accelerates faster. After 0.2 s, the tangential velocity of the bearing inner ring equals the tangential velocity of the rotor outer surface. As the pair of angular contact bearing has a higher mass and moment of inertia, the acceleration of the second bearing is lower.

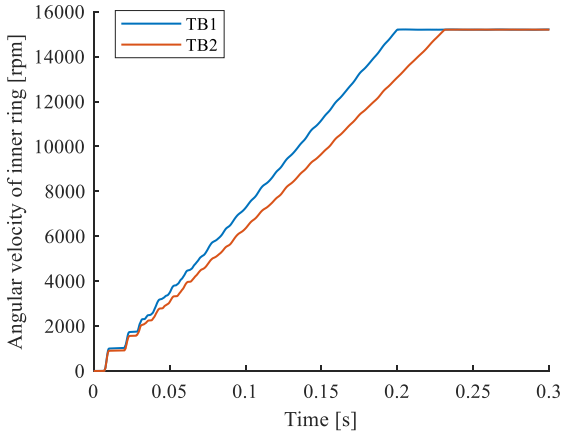

Fig. 11. Angular velocity of rotor and inner race during dropdown.

4.2 Effect of surface waviness

In order to evaluate the influence of the surface waviness on the friction heat generated in the touchdown bearings, the contact forces and the friction heat generation in the bearing has been evaluated for six different configurations that are introduced in Table 4. The first case presumes that the bearing has an ideal surface. In cases 2-4, the inner race has a surface waviness with the amplitude of 1 µm and the 1st, 2nd and 3rd orders of waviness are studied. The last two cases are used to evaluate the influence of a higher amplitude of surface waviness.

Table 4. Various cases of waviness in bearing.

Different cases of surface waviness in bearing, waviness order (Amplitude)						
	Ideal	1st (1 µm)	2nd (1 µm)	3rd (1 µm)	2nd (4 µm)	3rd (2 µm)
Ideal surface of bearing	✓	-	-	-	-	-
Waviness in both races	-	✓	✓	✓	✓	✓
Waviness in contact of rotor inner race	-	✓	✓	✓	✓	✓

4.2.1 Contact force

Figure 12 shows the contact force between the rotor and the bearing inner ring as functions of time. The waviness orders of the first to third orders (namely eccentricity, ellipticity and triangularity) are studied and compared with the bearing having the ideal geometry. In the simulation, the contact forces between individual balls and bearing races have been investigated. Then, the magnitudes of bearing force depicted in Fig. 13 are obtained based on the model presented in [35]. The first hit of the rotor on the bearings results in high contact forces exceeding 5000 N. After the first two hits, the rotor experiences lower bounces thus shorter time periods where rotor and inner ring are not in contact. Fig. 12-b shows a close zoom of the figure for the time span of 0.025 - 0.1 s. The figure shows that with the surface waviness of amplitude 1µm, the contact occurs in the time close to the bearing with the ideal surface and it does not cause noticeable change in the contact time of the rotor and touchdown bearing. Eventually, the rotor is in continuous contact with the bearing inner ring and the contact force between the rotor and the inner

ring gradually settles around 500 N. The difference of the bearing waviness can be seen actually at the time when the rotor is in continuous contact with the bearing. The waviness components affect the variation of the forces when the rotor is swinging smoothly on the bottom of the touchdown bearing. In the ideal case, the contact force between the rotor and inner ring settles at the level of 500 N soon after the first hits. In other cases where any order of bearing waviness is included, the contact force varies below or above the magnitude of the contact force in the ideal bearing. The magnitude of the variation can be as high as double the stabilized level of the contact force in the ideal case. The highest variation in contact forces between the rotor and the inner ring are in the case of triangular waviness where the contact force varies between 150 and 1000 N when the rotor is swinging on the bearings. Contradictorily, the contact forces in the bearing are evenly smooth in the case of triangular bearings and in ideal bearings (Fig.13). In cases of first and second order waviness, the contact forces in the bearing vary notably. A reason for such behavior is most likely geometrical. The triangularity of the bearing has a 120-degree phase difference between wave peaks that results in forces that are counteracting with respect to each other. In the case of a 180-degree phase difference in the waves, there are no such counteracting forces and the highest force component follows the wave peak traveling in the lower half of the bearing ring.

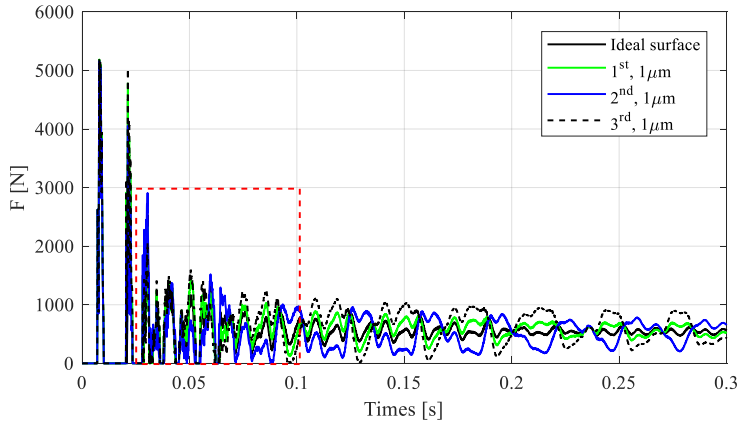

a)

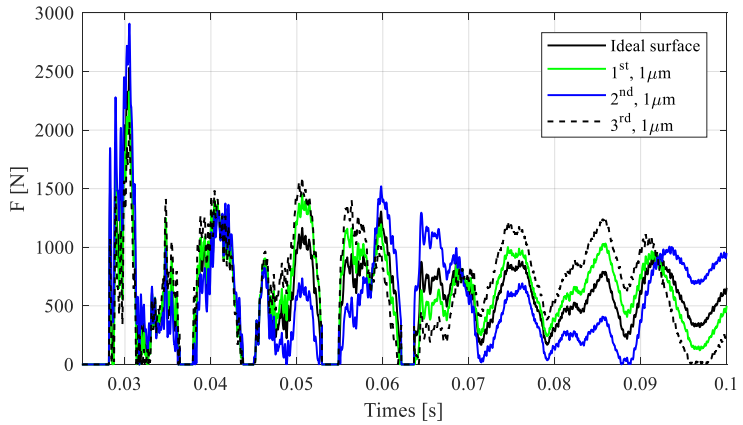

b)

Fig. 12. Magnitude of the contact force between the rotor and inner race for the bearing with the ideal surface and a bearing with waviness. a) simulation time 0.3s, b) zoomed view from 0.025 to 0.1s.

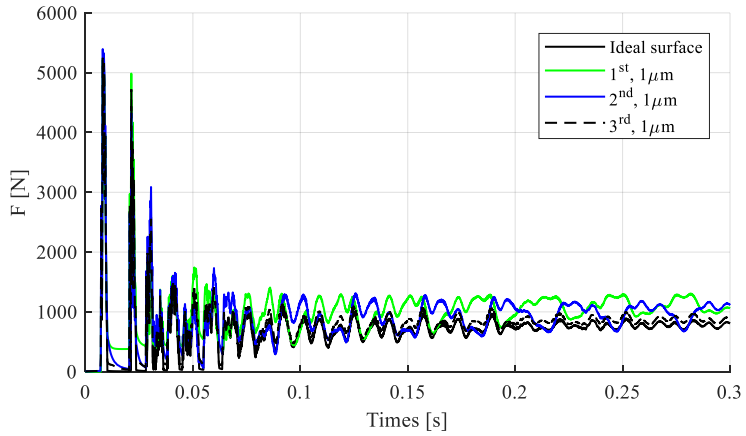

Fig. 13. The magnitude of the bearing force for the bearing with an ideal surface and bearing with waviness.

4.2.2 Friction heat generation

Fig. 14 (a) shows the friction torque in the touchdown bearing in the case of the ideal bearing surface. In this case study, the load-dependent friction torque is less than the velocity-dependent friction torque. In the first contact, the load-dependent friction has the highest value of about 0.14 Nm. After the second contact, it is reduced and gradually approaches a uniform level. The velocity-dependent term is highly affected by the angular velocity of the inner race and by increasing the angular velocity, the level of viscous friction torque rises. In the high-speed application, the velocity-dependent viscous friction term is the most determinative term in the calculation of global friction torque (equation 20). It is required to mention that applying the empirical equation for the velocity dependent fiction determined by Palmgren [42], equation (22), can raise some uncertainties in the calculation of the velocity dependent term in oil free touchdown bearing. Above equation is valid for the case where the bearing operates at moderate speed and does not carry excessive load and can be used for the oil with the specific gravity of 0.9. Therefore, it is necessary to investigate the influence of the velocity dependent term in the calculation of the power loss in the bearing. Later on, in section 4.2.3 it will be shown that the internal heat generation in the inner ring and outer ring is relatively low compared to the friction heat due to the contact of rotor and inner ring. Therefore applying the equation for the calculation velocity dependent term by Palmgren still can provide reasonable result for the dropdown of the rotor in oil free touchdown bearing. The velocity of the bearing inner ring increases constantly when the rotor is in contact resulting in a smooth friction torque curve. Fig. 14 (b) shows that for surface waviness with the amplitude of 1 µm, the global friction torque has a small variation irrespective of the waviness order, and the effect is negligible.

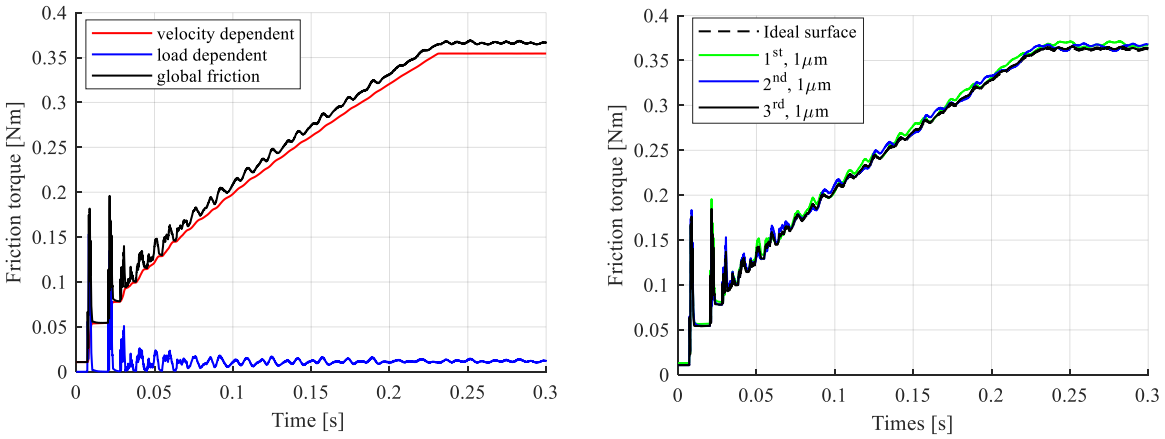

(a) (b)

Fig. 14. Friction torque in bearing a) ideal surface b) global friction torque for ideal surface and the bearing with 1–3 order waviness with the amplitude of 1µm.

The effect of the spinning velocity on the calculation of the total heat generation in the bearing race (equation 24) should be taken into account. The spinning torque of the ball which undergoes the highest contact stress is shown in Fig. 15. The spinning torque in the rotor drop is not uniform and in the first hit, the contact force between the ball and bearing race is high and in the following contacts, the spinning torque is reduced.

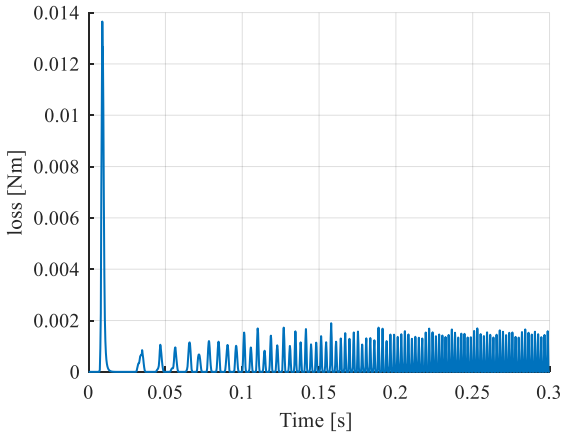

Fig. 15. The spinning loss due to the contact of the ball with the highest contact stress and the bearing race (Case I - Table 4).

4.2.3 Heat generation

Fig. 16 shows the heat generation in the bearing during a 0.3 second time span from the rotor drop. The figure shows that from the start of the dropdown until 0.2 s, the heat generation increases in both races; afterward it is stabilized around the constant value. In the case of the bearing with the ideal surface, the maximum heat generation in the contact of the outer race is 60 W; that is approximately 10 W higher than the maximum heat generation in the inner race. This figure reveals the heat generation in the bearing races has a similar trend to the acceleration of the bearing race (Fig. 11). In addition, for the surface waviness with the amplitude of 1µm, regardless of the waviness order, the heat generation in the bearing is higher than the bearing with the ideal surface. In the case of first order waviness, the maximum heat generation in the bearing races is about 10 % higher than the

corresponding values for the bearing with the ideal surface. In the same amplitude of surface waviness, for the higher order of waviness (2^{nd}, 3^{rd}), the difference in the heat generation of the bearing with surface waviness and the ideal surface are reduced to approximately 7% and 5 %, respectively. Furthermore, at the start of dropdown the difference between the heat generation in the bearing with surface waviness and the bearing with the ideal surface is low and as the rotor starts to rub against the touchdown bearing, the difference will be higher; after 0.2 s the difference in the heat generation of the bearing with surface waviness and ideal case reaches to the maximum value.

As demonstrated in [16], the global friction torque in the bearing is divided into the friction torque in the inner ring and outer ring. Due to the smaller radius of the inner race rather than the outer race radius, the friction torque in the inner race (The term M_{ij} in equation 24) is less than the friction torque in the outer race. Therefore, the inner race experiences less heat generation compared to the outer ring. As mentioned earlier, the heat generation in the bearing races is dependent on the friction torque and the angular velocity of the bearing component. Just after the dropdown, the touchdown bearing experiences a high contact force and at this time the angular velocity of the inner ring is still low. For this reason, in the first few milliseconds of the simulation, the main part of the global friction torque is due to the load-dependent friction torque. When the inner ring accelerates because of the high angular velocity of the inner ring, the friction drag torque increases. In addition, the friction drag torque is expressed in terms of the angular velocity of the inner ring. For this reason, the heat generation in the bearing follows the same trend as the acceleration of the inner ring. Moreover, when the surface waviness exists in the bearing, the overall magnitude of the contact force in the bearing is higher compared to the bearing with the ideal surface. After the inner ring rotates at the same speed as the rotor, a clear fluctuation in the magnitude of the heat generated in the bearing is observed. This can be attributed to the nature of the sinusoidal function used for the numerical simulation of the waviness.

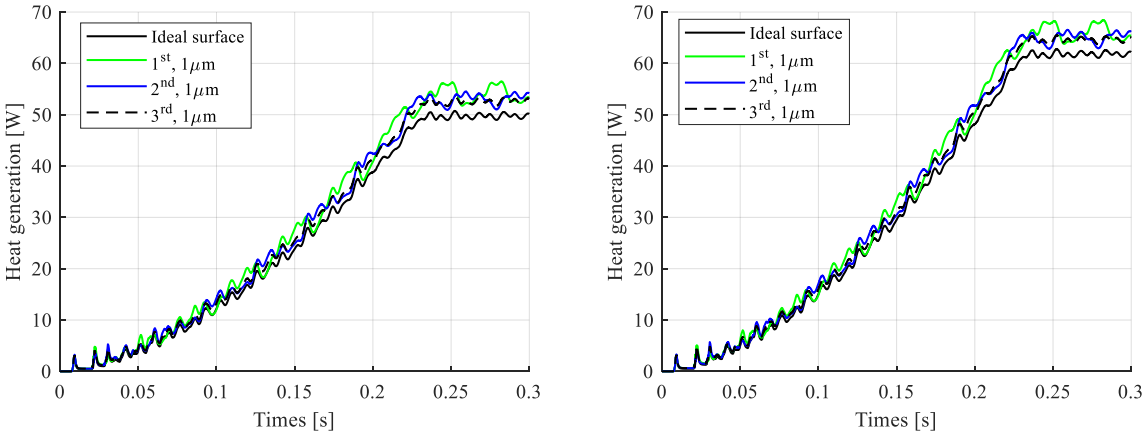

Fig. 16. Internal heat generation in the touchdown bearing a) inner ring b) outer ring.

Figure 17 depicts the frictional heat generation that is created during the contact between the rotor and the touchdown bearings. The figure shows that a few milliseconds after the dropdown, the heat generation in the bearing with the ideal surface rises to the maximum value of $2.8 \cdot 10^4$ W. Then it is reduced and for a couple of milliseconds becomes zero. Then, the second peak in the heat generation is observed. Afterward, the reduction in

the heat generation is followed by a fluctuation until 0.2. Then, the heat generation becomes zero. The overall pattern shows that waviness imperfection results in greater amount of heat generation between the rotor and inner ring rather than the bearing with the ideal surface.

When the magnetic field fails, a few milliseconds will pass before the rotor drops and contacts the touchdown bearing. At this time, the rotor does not have contact with the inner ring and therefore in the start of the dropdown, the heat generation between the rotor and inner ring is zero. Due to the high magnitude of the contact force between the rotor and inner race, and also the high magnitude of the relative angular velocity of the rotor and inner race, the heat generation in the first contact of the rotor and inner race were found to be considerably greater than internal heat generated in the bearing. When the rotor bounces for a second time, there is no physical contact between the rotor and touchdown bearing. Therefore, the heat generation again becomes zero. As the inner ring accelerated with the same speed as the rotor (after 0.2 s), the relative velocity between the rotor and inner ring becomes zero. Therefore, the heat generation is equal to zero.

The surface waviness in the bearing results in greater penetration of the rotor in the inner ring. Consequently, the contact force increases and the bearing has to endure higher heat generation. Even though the magnitudes of the peak values are very high, the time periods for the highest peaks are is just some milliseconds, resulting in a moderate rise in temperatures, as will be shown in the next section.

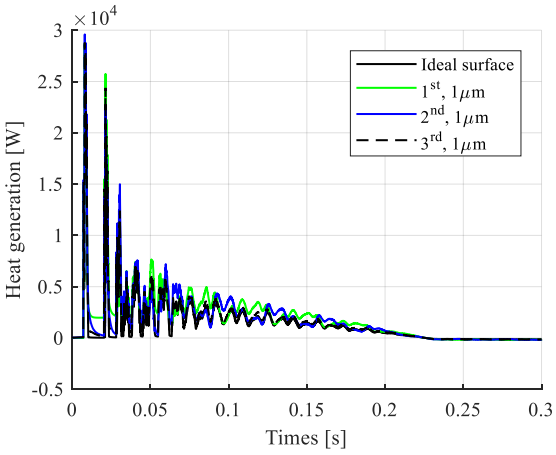

Fig. 17. Friction heat generation in the contact of rotor and touchdown bearing.

4.3 Thermal analysis

First, the thermal analysis of the bearing has been studied for the case where the bearing has an ideal surface. Fig. 18 shows the temperature rise for different nodes of the model introduced in Fig. 6 during the 0.3 s time span after the dropdown. This figure shows that in the dropdown, the temperature of bearing races, ball, the contact area of the ball and bearing races, housing as well as the rotor, is increased. Nevertheless, the thermal expansion of different components of the bearing and rotor are dissimilar. For the few milliseconds after the dropdown, the temperature of the inner ring is the same as ambient temperature; then the sudden increase in the temperature is observed. Afterward, for the second time, the temperature of the inner ring remains constant and instantaneously rises. This behavior continues until gradually the temperature reaches the maximum value of 296.2 K at 0.2s.

Then, the temperature stabilizes. A similar pattern has been observed for the temperature of the shaft. However, the maximum temperature of the shaft is approximately six times less than the maximum temperature of the inner ring. In the contact point of the ball and bearing race, the temperature increases rapidly to just slightly above the maximum temperature of the inner ring and then remains almost constant. During the simulation time of 0.3 s, the temperature of the ball and outer race increases to 294.5 and 293.2 K, respectively. The bearing housing does not experience a significant rise in temperature and remains close to 293 degrees.

It should be noted that the temperature rise in the bearing is not a linear phenomenon. The rotor drop speed, geometry and material property of the rotor and bearing, the air gap clearance, as well as the friction in the bearing, can influence the temperature of the rotor and touchdown bearing. In the beginning of the dropdown, the rotor moves downwards; at this time the rotor is not in contact with the touchdown bearing. For this reason, during the first few milliseconds, the temperature of the inner ring is the same as the ambient temperature. After the initial contact, there is a considerable friction heat generation between the rotor and inner ring which can explain the instantaneous increase in the temperature of the inner race. After the first contact of the rotor and inner ring, the rotor bounces back; at this time the temperature remains constant until the rotor contacts the bearing for a second time. This behavior lasts until the rotor continually whirls in the bearings. The temperature of the inner ring increases in relation to the acceleration of the bearing race. When the inner ring accelerates, the temperature of the inner ring increases and when it rotates with the same angular velocity as the rotor (from 0.2s to end of simulation), the heat generation remains constant and the temperature of the inner ring stabilizes. The high friction between the bearing and rotor, and also the friction inside bearing, makes the temperature in the contact region of the ball and bearing race and ball be high. In addition, it is clear from Fig. 6 that in the thermal model of the bearing, the lumped mass of the shaft is significantly greater than the lumped mass of bearing components. Therefore, the temperature of the rotor increased at a lower rate rather than the bearing. Inside the bearing housing, the heat transfers via conduction and the natural convection occurs between the outer face of the housing and environment. Therefore, the temperature rise is lower than in other parts and there is not a significant difference in the temperature rise.

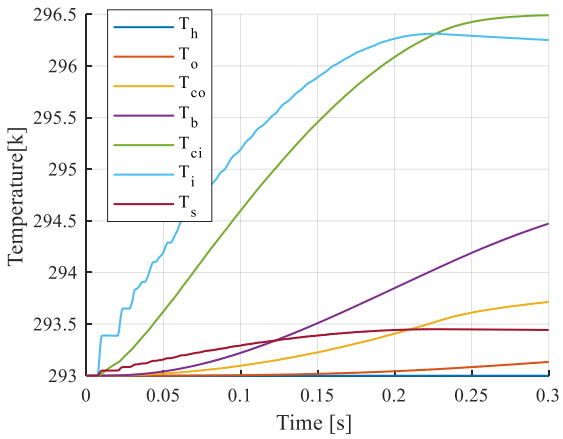

Fig. 18. Temperature rise in the rotor (T_s), inner ring (T_i), outer ring (T_o), ball (T_b), housing (T_h), contact of the ball and bearing races (T_{ci},T_{co}).

The results can be partially validated based on the existing literature on the rotor dropdown. The trend in the temperature increase of the inner race is found to be similar to Jin et al. [17] and Zhao et al. [16]. In the start of dropdown, a sharp increase in the temperature of the inner ring has been observed. Then the temperature increase until a maximum level is reached. In their study, the maximum temperature rise of the inner ring was approximately 6 C, which is in line with results of this study. In the simulation it is shown that high contact force between rotor and inner ring occurs for a very short moment (mainly in first contact) and a similar finding was reported by Zhao [16].

Fig. 19 (a) presents the temperature rise of the inner race for the different amplitude of surface waviness. In the circumstance where the bearing suffers from surface waviness regardless of either the amplitude of waviness or the waviness order, the temperature of the inner ring is higher than the temperature of the bearing with the ideal surface. For the surface waviness with the amplitude of 1 µm, the first order waviness results in a higher temperature rise rather than the higher order of waviness. In order to observe the influence of the higher amplitude of surface waviness in the temperature rise of the bearing, the last two cases, 2 µm (3^{rd}) and 4µm (2^{nd}), has been also studied. The highest studied amplitude for the surface waviness is 4 µm, which is within the range of the surface waviness of bearings with best bearing manufacturing conditions reported in [45]. The higher amplitude of surface waviness (2 µm, 3^{rd}) leads to more temperature rise in the inner ring. For the bearing with the ideal surface, the temperature rise is 3.5 degrees, whereas for the last case (4 µm, 2^{nd}) the temperature of the inner race has an 8º K increase. A similar pattern has been found for the temperature rise of the contact area of the ball and the inner ring (Fig. 19 (b)). The previous section showed that in the case of surface waviness with the amplitude of 1 µm, the waviness orders 1–3 causes a minor change in friction heat generation. Consequently, the temperature of the inner ring experiences a small increase (approximately 1º K) when compared to the bearing with the ideal surface. With the higher amplitude of the waviness, there are noticeable increases in the contact force and power loss in the bearing. For this reason, the temperature of the inner ring rises noticeably higher than the bearing with the ideal surface. In addition, when both races have waviness, the contact force and the power loss is higher than the case where only one race has waviness.

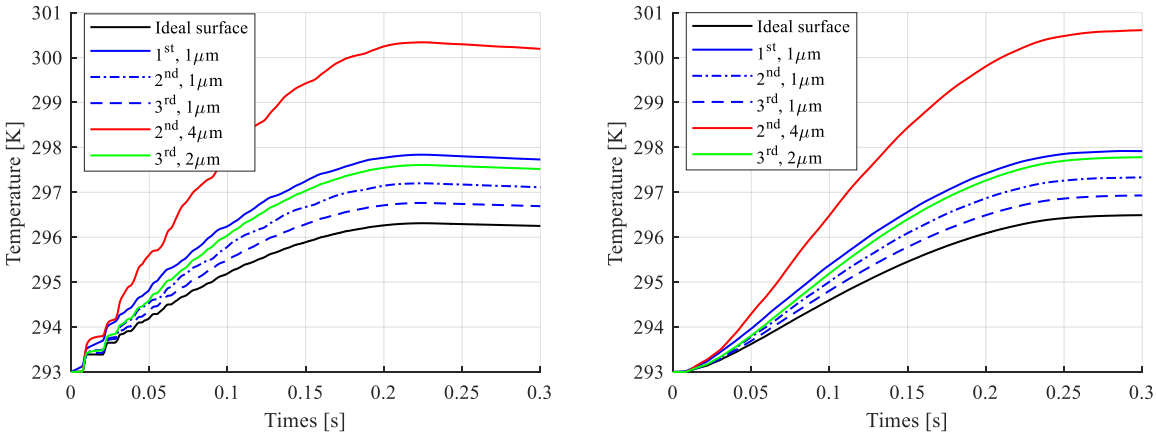

a) b)

Fig. 19. Temperature rise of the inner ring and the contact area of ball/inner ring for both ideal surface and the various order and magnitude of surface waviness; a) inner ring b) contact point of ball inner ring.

5 CONCLUSION

In this study, the dynamic and thermal model of touchdown bearings in a rotor drop were presented. In the simulation, the FE-model of the flexible rotor was integrated with the dynamic model of the touchdown bearing. The contact forces between the rotor and safety bearing, as well as internal contact force in the touchdown bearing, were calculated by Hertzian contact theory. The friction heat generated due to impact, whirling of the rotor on the touchdown bearing, and the internal friction torque in the bearing were obtained. The one-dimensional equivalent electrical circuit model is applied to the thermal model of the touchdown bearing. The orbital motion of the rotor showed that the higher dynamic friction coefficient between the rotor and touchdown bearing increases the arc of the contact region which the rotor settles in the bearing. The results showed that the temperature rise in the bearing is influenced by the variation of the angular velocity of the rotor and inner ring, viscosity of lubrication and the friction between the rotor and touchdown bearing, as well as the friction inside the bearing. Moreover, differences in surface waviness in the bearing have been studied. It has been found that for a small amplitude of surface waviness, the various orders of surface waviness result in small changes in the contact force and heat generation in the bearing. The results indicated that the amplitude of the waviness has a greater effect on increasing the power loss and contact forces between balls, and also the contact of the rotor and inner race. Meanwhile, for the constant amplitude of the waviness, the higher waviness order does not lead to a considerable change in the results.

Acknowledgment

The authors would like to thank Academy of Finland for funding under the ViDROM project (grant number 277502).

References

[1] Kärkkäinen A, Sopanen J, Mikkola A. Dynamic simulation of a flexible rotor during drop on retainer bearings. Journal of Sound and Vibration 2007;306:601-17.

[2] Ecker H. Nonlinear stability analysis of a single mass rotor contacting a rigid backup Bearing. Proceedings of the Euromech Collaquium 15-18, Loughborough, UK 1998:79-88.

[3] Taylor HD. Rubbing shafts above and below resonant speed. GE Technical Information Series 1924: No. 16709.

[4] Newkirk BL. Shaft rubbing. Mechanical Engineering 1926:48:830-32.

[5] Childs DW. Rub induced parametric excitation in rotors. Journal of Mechanical Design 1979:10:640-4.

[6] Choy FK, Padovan J. Non-linear transient analysis of rotor-casing rub events. Journal of Sound and Vibration 1987;113:529-45.

[7] Muszynska A. Partial lateral rotor to stator rubs. Proceedings of the Institution of Mechanical Engineers 1984: C281/84.

[8] Keogh PS. Contact dynamic phenomena in rotating machines: Active/passive considerations.

Mechanical Systems and Signal Processing 2012;29:19-33.

[9] Keogh PS, Yong WY. Thermal assessment of dynamic rotor/auxiliary bearing contact events. ASME Journal of Tribology 2007;129:143-52.

[10] Liu T, Lyu M, Wang Z, Yan S. An identification method of orbit responses rooting in vibration analysis of rotor during touchdowns of active magnetic bearings. Journal of Sound and Vibration 2018: 414: 174-191.

[11] Schmied J, Pradetto JC. Behaviour of a one ton compressor rotor being dropped into the auxiliary bearings. Proceeding of the third international symposium on magnetic bearings, Alexandria. 1992:145-156.

[12] Burton RA, Staph HE. Thermally activated seizure of angular contact bearings. Tribology Transactions 1967;10:408-17.

[13] Takabi J, Khonsari MM. On the thermally-induced failure of rolling element bearings. Tribology International 2016;94:661-74.

[14] Sun G. Auxiliary bearing life prediction using Hertzian contact bearing model. ASME Journal of Vibration and Acoustics 2006;128:203-9.

[15] Lee JG, Palazzolo A. Catcher bearing life prediction using a rainflow counting approach. ASME Journal of Tribology 2012;134.

[16] Zhao Y, Yang G, Shi Z, Zhao L. Thermal Analysis and Simulation of Auxiliary Bearings and Its Application in the High Temperature Reactor-10. Journal of Tribology 2016;138.

[17] Jin C, Zhu Y, Xu L, Xu Y, Zheng Y. The thermodynamic properties of a new type catcher bearing used in active magnetic bearings system. Applied Thermal Engineering 2015;82:253-63.

[18] Sun G. Rotor drop and following thermal growth simulations using detailed auxiliary bearing and damper models. Journal of Sound and Vibration 2006;289:334-59.

[19] Takabi J, Khonsari MM. Experimental testing and thermal analysis of ball bearings. Tribology International 2013;60:93-103.

[20] Neisi N, Sikanen E, Heikkinen JE, Sopanen J. Effect of off-sized balls on contact stresses in a touchdown bearing. Tribology International 2018; 120:340-9.

[21] Jin C, Wu B, Hu Y. Heat generation modeling of ball bearing based on internal load distribution. Tribology International 2012;45:8-15.

[22] Yan K, Wang N, Zhai Q, Zhu Y, Zhang J, Niu Q. Theoretical and experimental investigation on the thermal characteristics of double-row tapered roller bearings of high speed locomotive. International Journal of Heat and Mass Transfer 2015;84:1119-30.

[23] Ai S, Wang W, Wang Y, Zhao Z. Temperature rise of double-row tapered roller bearings analyzed with the thermal network method. Tribology International 2015;87:11-22.

[24] API. Axial and Centrifugal Compressors and Expander-Compressors for Petroleum, Chemical and Gas Industry Services (Standard API 617) American Petroleum Institute, USA, 2002.

[25] Zhuo Y, Zhou X, Yang C. Dynamic analysis of double-row self-aligning ball bearings due to applied loads, internal clearance, surface waviness and number of balls. Journal of Sound and Vibration 2014;333:6170-89.

[26] Harsha SP, Kankar PK. Stability analysis of a rotor bearing system due to surface waviness and number of balls. International Journal of Mechanical Sciences 2004;46:1057-81.

[27] Wardle FP. Vibration forces produced by waviness of the rolling surfaces of thrust loaded ball bearings Part 1: Theory. Proceedings of the Institution of Mechanical Engineers, Part C: Journal of Mechanical Engineering Science 1988;202:305-12.

[28] Wardle FP. Vibration Forces Produced by Waviness of the Rolling Surfaces of Thrust Loaded Ball Bearings Part 2: Experimental Validation. Proceedings of the Institution of Mechanical Engineers, Part C: Journal of Mechanical Engineering Science 1988;202:313-9.

[29] Changqing B, Qingyu X. Dynamic model of ball bearings with internal clearance and waviness. Journal of Sound and Vibration 2006;294:23-48.

[30] Liu W, Zhang Y, Feng Z, Zhao J, Wang D. A study on waviness induced vibration of ball bearings based on signal coherence theory. Journal of Sound and Vibration 2014;333:6107-20.

[31] Heikkinen JE, Ghalamchi B, Viitala R, Sopanen J, Juhanko J, Mikkola A, Kuosmanen P. Vibration analysis of paper machine's asymmetric tube roll supported by spherical roller bearings. Mechanical Systems and Signal Processing 2018;104:688-04.

[32] Halminen O, Aceituno JF, Escalona JL, Sopanen J, Mikkola A. A touchdown bearing with surface waviness: A dynamic model using a multibody approach. Proceedings of the Institution of Mechanical Engineers, Part K Journal of Multi-body Dynamics 2017:231;658-69.

[33] Halminen O, Aceituno JF, Escalona JL, Sopanen J, Mikkola A. A touchdown bearing with surface waviness: Friction loss analysis. Mechanism and Machine Theory 2017;110:73-84.

[34] Nelson HD. A Finite Rotating Shaft Element Using Timoshenko Beam Theory. ASME Journal of Mechanical Design 1980:102(4), 793-803.

[35] Sopanen J, Mikkola A. Dynamic model of a deep-groove ball bearing including localized and distributed defects. Part 1: Theory. Proceedings of the Institution of Mechanical Engineers Part, K Journal of Multi-body Dynamics 2003;217:201-11.

[36] Hunt K, Crossley F. Coefficient of restitution interpreted as damping in vibroimpact. ASME Journal of Applied Mechanics 1975: 42(2): 440-5.

[37] Krämer E. Dynamics of Rotors and Foundations. Springer-Verlag, Berlin 1993.

[38] Eschmann HW. Ball and Roller Bearings: Theory, Design and Application. Second edition. Wiley 1985.

[39] Hamrock BJ, Dowson D. ball bearing mechanics. 1981, NASA Technical Memorandum 81691.

[40] Nguyen-Schäfer, Hung Computational Design of Rolling Bearings : Springer International Publishing, 2016.

[41] Harris TA. Rolling bearing analysis. 4th ed. New York: John Wiley & sons, 2001.

[42] Palmgren A. Ball and Roller Bearing Engineering, 3rd ed., Burbank, Philadelphia 1959: 34-41.

[43] Poritsky H, Hewlett CW, Coleman RE. Sliding friction of ball bearings of the pivot type. Journal of Applied Mechanics. 1947;14:261-8.

[44] Heikkinen J, Smirnov A, Hakonen V, Sopanen J. Virtual Testing of AMB Supported Rotor-system. 2015:465-71.

[45] Mohanty AR. Machinery condition monitoring principal and practice : CRC Press, Taylor & Francis, 2015.